



Contents lists available at ScienceDirect

International Journal of Rock Mechanics and Mining Sciences

journal homepage: www.elsevier.com/locate/ijrmms

Hydraulic fracturing with leakoff in a pressure-sensitive dual porosity medium

Jiehao Wang^{a,*}, Derek Elsworth^a, Martin K. Denison^b^a Department of Energy and Mineral Engineering, Pennsylvania State University, University Park, PA 16802, USA^b Reaction Engineering International, Salt Lake City, UT, USA

ARTICLE INFO

Keywords:

Hydraulic fracturing
Proppant transport
Leakoff
Dual porosity media
Pressure-sensitive permeability
Naturally fractured reservoir

ABSTRACT

Hydraulic fracturing is a key method in the stimulation of shale gas reservoirs. Shale gas formations often contain natural fractures which are fluid-pressure sensitive and dilate in response to the inflation of the fracture, increasing fluid loss and slowing down and potentially prematurely arresting fracture propagation. Models typically assume 1-D single-porosity/permeability (Carter) leakoff perpendicular to the hydraulic fracture. However, the leakoff process in naturally fractured formations is considerably more complex. In this study, we present an hydraulic fracturing model based on the PKN-formalism which accommodates leakoff into a pressure-sensitive dual porosity medium. Proppant transport is accommodated by introducing empirical constitutive equations to determine the proppant distribution during the hydraulic fracturing treatment. The model is solved numerically and is validated against known small and large time asymptotic solutions. The model is capable of providing a rapid estimation of the morphology of hydraulic fractures in naturally fractured formations and the corresponding proppant distribution. The simulation results illustrate that the leakoff into a dual porosity medium, where fracture permeability is a strong function of applied fluid pressure, results in a reduced length of the propagating fracture due to the fugitive fluid leakoff from the fracture into the surrounding formation and that this in turn results in a reduced maximum width during the treatment. The ability to infuse proppants in fluid-driven fractures penetrating large distances from the injection wellbore is further limited by premature screen-out. This may compromise the ultimate efficiency of the final hydraulic fracture regarding gas recovery. Reduced propagation and premature screen-out are limited by low permeability and large spacing of the natural fractures. The presence of an existing network of natural fractures, including those adjacent to the hydraulic fracture that may become propped, aids in the recovery of the resource by reducing diffusion lengths of the hydrocarbon to the main fracture.

1. Introduction

Hydraulic fracturing is performed by injecting highly pressurized fluid into subsurface to fracture the formation. Proppant is introduced later to keep the fractures open. Since the pioneering work of Khristianovic and Zheltov,¹ various models have been proposed to approximately define the development of fracture geometry, among which the PKN and GDK models are the most popular.^{1–4} Those models including their numerical solutions have been reviewed by Adachi et al.⁵ and Rahman and Rahman.⁶ Further studies have been devoted to understanding the regimes of propagation and near tip behavior^{7–11} which are summarized by Detournay.¹²

A vertical hydraulic fracture will remain at approximately constant height if the contrast in horizontal stress between pay zone and bounding zones is sufficiently high, as shown in Fig. 1. A model with

constant height is of sufficient interest when the pay zone includes only one layer in the formation, although many models consider the growth of the fracture height.^{13–15} In the constant height case, when the half-length of the hydraulic fracture, l , is much larger than its height, H , the propagation process can be described using the classical PKN hydraulic fracturing model.^{2,3} In this model, the fracture propagates laterally away from the borehole. The volume of the propagating fracture exactly balances the input of the fracturing fluid with the (i) advance of the fracture tip, (ii) its concurrent inflation, and (iii) leak-off into the formation. It achieves this by transporting fluid within and along the fracture. Typically, 1-D single-porosity/permeability leakoff perpendicular to the hydraulic fracture^{16,17} is assumed in the hydraulic fracture models representing the formation as a single-porosity porous medium.

However, shale reservoirs are typically naturally fractured at a variety of length-scales. These lengths vary from microfractures at the

* Corresponding author.

E-mail addresses: jiehao.wang@psu.edu (J. Wang), elsworth@psu.edu (D. Elsworth), denison@reaction-eng.com (M.K. Denison).

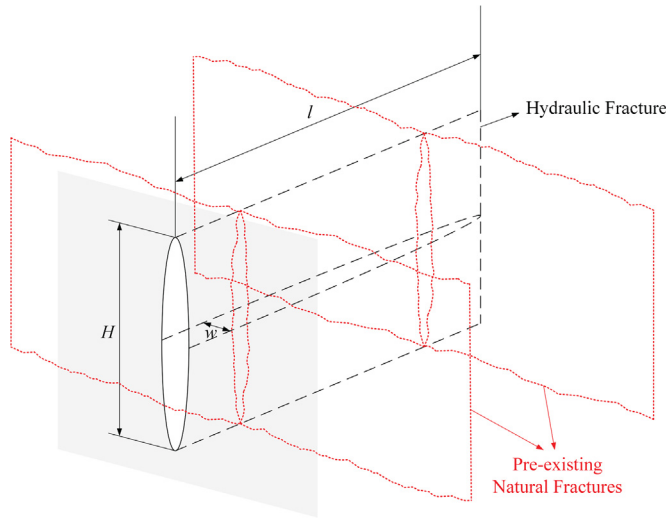


Fig. 1. Schematic of the main PKN fracture crossing natural fractures.

scale of tens of microns to observable fractures at the centimeter to meter scale and are compounded by the presence of faults at decameter to fractions of a kilometer scale. The porous matrix and transecting fractures have very different mechanical and transport properties. The fractures are mechanically soft and weak in tension, and serve as ready defects for the concentration of deformation by inflating/propagating fluids. The pre-stimulation differential in the transport properties of the shale is further modified by the presence of such driven hydraulic fractures. The permeability of the shale fractures may be significantly increased by their dilation and retained in this dilated state by the potential infusion of proppant. Therefore, the leakoff process in naturally fractured shale formations during the treatment is considerably more complex. In this paper, we present a hydraulic fracturing model based on the PKN-formalism which accommodates the leakoff into naturally fractured formations. This model considers the naturally fractured formation as a dual porosity medium, with the leakoff process on dual time scales - early leakoff dominated by fracture dilation and a delayed leakoff dominated by mass transfer from activated natural fractures to the matrix. In this, the later effect may play an important role if the matrix is dissected with a short separation between natural fractures.^{18,19} This dual porosity leakoff may increase the fluid leakoff volume and prematurely arrest fracture propagation, which in turn may significantly influence the ability to infuse proppants into the accessed reservoir at desired large distances from the injection wellbore. A proppant transport model is followed to investigate this effect.

The basic equations governing the response of a PKN fracture, the leakoff process in the dual porosity medium, and the proppant transport within evolving fractures are summarized in Section 2. Numerical algorithms to solve this proposed model are introduced in Section 3. In Section 4, the proposed model and algorithms are validated, and several simulations are performed to demonstrate the effect of dual porosity leakoff on fracture propagation and proppant transport.

2. Mathematical formulation

2.1. The Perkins-Kern-Nordgren (PKN) model

Transient evolution of the fracture length and aperture is predicted by the PKN model, given the injection rate, Q_0 , the fracture height, H , Young's modulus, E , and Poisson's ratio, ν , of the rock, the fluid viscosity, μ , and the leak-off velocity, $u(x,t)$. It is assumed that the cross-section of fracture is elliptical, that the pressure in the fracture is uniform over the height of the fracture, and that the in situ stress acting perpendicular to the plane of the fracture, σ_{\min} , is constant over the

entire fracture. An approximation is made that plain strain prevails in planes perpendicular to the propagation direction. These assumptions enable the model to be formulated in terms of an average aperture, and an average flux $\bar{q}(x, t)$ defined as

$$\begin{cases} \bar{w}(x, t) = \frac{1}{H} \int_{-H/2}^{H/2} w(x, z, t) dz \\ \bar{q}(x, t) = \frac{1}{H} \int_{-H/2}^{H/2} q(x, z, t) dz \end{cases} \quad (1)$$

The relationship between local flux $q(x,z,t)$ and pressure gradient is approximated by Poiseuille's law written as¹⁵

$$q(x, z, t) = -\frac{w^3(x,z,t)}{12\mu} \frac{\partial p(x,t)}{\partial x}, \quad -\frac{H}{2} < z < \frac{H}{2}. \quad (2)$$

By considering the elliptical shape of the aperture profile, integrating Eq. (2) over H yields

$$\bar{q}(x, t) = -\frac{\bar{w}^3(x, t)}{\pi^2 \mu} \frac{\partial p(x, t)}{\partial x}. \quad (3)$$

The assumption of plain strain in planes perpendicular to the propagation direction allows the nonlocal relationship between aperture and net pressure to be reduced to a local operator of the form

$$\bar{w}(x, t) = \frac{\pi H}{2E'} p(x, t), \quad (4)$$

where $E' = E/(1 - \nu^2)$ is the plane strain Young's modulus and $p(x, t) = p_{\text{fluid}}(x, t) - \sigma_{\min}$ is the net fluid pressure inside the fracture with $p_{\text{fluid}}(x, t)$ being the absolute fluid pressure. Note that the plane strain approximation is true only at distance $O(H)$ or more away from fracture tip and when the fracture width and pressure vary smoothly along the fracture length direction. In addition, the plane strain approximation constrains the application of the model to situations where the toughness of the rock is negligible. These two limitations of the model can be overcome by introducing a non-local elasticity equation.¹⁰

By considering fracture inflation and fluid leakoff, the local fluid mass balance equation is written as

$$\frac{\partial \bar{q}(x, t)}{\partial x} + \frac{\partial \bar{w}(x, t)}{\partial t} + u(x, t) = 0, \quad (5)$$

where $u(x,t)$ is the fluid leakoff velocity accounting for both sides of the fracture. The classical Carter leakoff theory¹⁶ assumes that, for a given formation, the fluid leakoff velocity is perpendicular to the hydraulic fracture plane and is only a function of the time that the fracture wall is exposed to the fracturing fluid. This can be described as

$$u(x, t) = \frac{2C_l}{\sqrt{t - \tau(x)}}, \quad (6)$$

where the constant C_l is the leakoff coefficient, t is the lapse time since pumping starts, and $\tau(x)$ is the arrival time of the fracture tip at location x . However, for naturally fractured formations, which might be treated as dual porosity media, the leakoff process is considerably more complex and will be discussed in Section 2.2.

The fracture length $l(t)$ is not known a priori and is absent from the local mass balance equation (Eq. (5)). An equation for $l(t)$ is obtained by integrating Eq. (5) in space over the length of the fracture and then in time over the total lapsed time

$$\int_0^{l(t)} \bar{w}(x, t) dx + \int_0^t \int_0^{l(t')} u(x, t') dx dt' - \int_0^t q_0(t') dt' = 0, \quad (7)$$

where $q_0 = Q_0/(2H)$ is the fluid injection rate per unit height of fracture. In this global mass balance equation, we note that the first term is the total volume of the fracture and the second term is the cumulative fluid leakoff volume, with the last term accounting for the total fluid injection volume.

2.2. Governing equations for leakoff process in a dual porosity medium

The naturally fractured formation is considered as a dual porosity medium. Although sealed natural fractures cannot contribute to reservoir storage or enhance permeability at the beginning of the hydraulic fracturing treatment, they may reactivate and dilate after the treatment pressure reaches a critical fissure opening pressure, resulting in an exponential increase in fracture permeability with increased treatment pressure. Then, the fluid that flows into the natural fractures is dissipated by fluid loss into the newly exposed matrix surrounding the natural fractures.^{18,19} The governing equations for leakoff in a dual porosity medium and a dynamic fracture permeability model are summarized in the following.

The mass balance equations for fluid flow in matrix and natural fracture system, respectively, are

$$\frac{\partial M_m}{\partial t} + \nabla \cdot (\rho \mathbf{q}_m) = \omega(p_f - p_m)\rho, \tag{8}$$

$$\frac{\partial M_f}{\partial t} + \nabla \cdot (\rho \mathbf{q}_f) = -\omega(p_f - p_m)\rho, \tag{9}$$

where M is the fluid mass, ρ is the fluid density, \mathbf{q} is the flow rate, and p is the fluid pressure. The subscripts represent m for matrix and f for fracture, respectively. Eqs. (8) and (9) are solved in the domain of the formation surrounding the hydraulic fracture. For simplicity, transfer between matrix and surrounding natural fractures^{20–22} is quantified by the assumption of a quasi-steady response. Note that, in the context of hydraulic fracturing, flow between matrix and natural fractures may approach but not actually reach the quasi-steady state due to the short duration of the stimulation. Thus, using a model which can capture the early time response may be both more appropriate and more accurate.²³ However, fluid transfer at quasi-steady state is governed by the instantaneous pressure differential, $p_f - p_m$, and the transfer coefficient, ω , defined as

$$\omega = \frac{\pi^2 k_m}{s^2 \mu}, \tag{10}$$

where s is the spacing between fractures and k_m is the permeability of the matrix. Eq. (10) is for the case with one set of natural fractures (slab geometry) and assumes a quasi-steady state with constant pressure boundary condition. The interested reader may find a detailed explanation of this transfer coefficient in the literature.^{21,22}

It is assumed that fluid flow within both matrix and natural fracture system follow Darcy's law described as

$$\mathbf{q}_m = -\frac{k_m}{\mu} \nabla p_m, \tag{11}$$

$$\mathbf{q}_f = -\frac{k_f}{\mu} \nabla p_f. \tag{12}$$

By substituting Eqs. (11 and 12) into Eqs. (8 and 9) and considering that $M = \rho\phi$, the governing equations for fluid flow within matrix and natural fracture system, respectively, are obtained as (see Appendix A)

$$\left(\frac{\phi_m}{K_w} + \frac{1 - \phi_m}{K_s}\right) \frac{\partial p_m}{\partial t} + \nabla \cdot \left(-\frac{k_m}{\mu} \nabla p_m\right) = \omega(p_f - p_m), \tag{13}$$

$$\frac{\partial \phi_f}{\partial t} + \frac{\phi_f}{K_w} \frac{\partial p_f}{\partial t} + \nabla \cdot \left(-\frac{k_f}{\mu} \nabla p_f\right) = -\omega(p_f - p_m), \tag{14}$$

where ϕ_m and ϕ_f are the porosity of the matrix and natural fracture system, respectively, K_w is the fluid bulk modulus and K_s is the solid grain bulk modulus.

At the beginning of the hydraulic fracturing treatment, the natural fractures remain closed and sealed indicating that the permeability and porosity of the natural fracture system remain unchanged. As the treatment pressure increases, the potential exists for natural fractures to

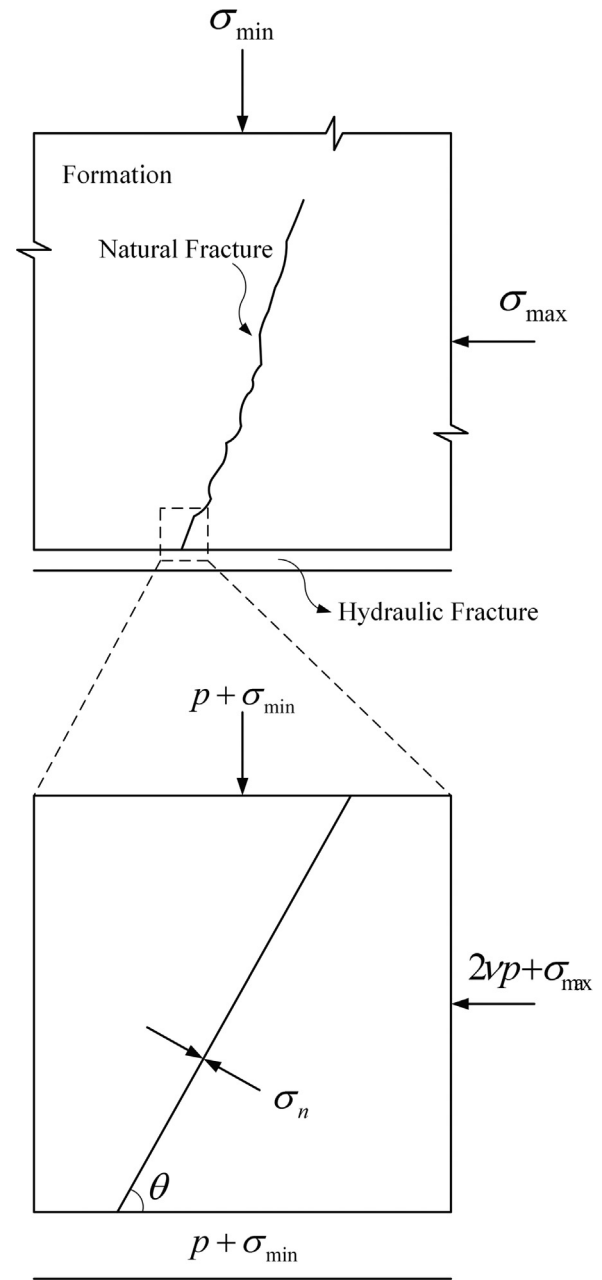


Fig. 2. Critical pressure to open natural fractures (p is net pressure in the hydraulic fracture, and σ_{\min} and σ_{\max} are maximum and minimum in-situ stresses, respectively).

reactivate and dilate. It is assumed that the natural fracture will open when the internal pressure exceeds the normal stress tending to close it,¹⁸ as illustrated in Fig. 2. In other words, the natural fracture reactivates when the effective normal stress $\sigma_n^e = \sigma_n - p_f \leq 0$, where σ_n is the total normal stress and p_f is the pressure within the natural fracture. Fig. 2 shows a rock element with dimensions that are small compared with the height of the hydraulic fracture. For the assumption of plane strain, during the hydraulic fracturing process, the stress in the direction parallel to the hydraulic fracture will increase by an amount of $2\nu p$, while the vertical stress increases by p , where p is the net pressure in the hydraulic fracture.¹⁸ Therefore, the effective normal stress can be calculated as

$$\sigma_n^e = \alpha_f p_f - [(2\nu p + \sigma_{\max}) \sin^2 \theta + (p + \sigma_{\min}) \cos^2 \theta], \tag{15}$$

where α_f is the Biot coefficient, σ_{\max} and σ_{\min} are maximum and

minimum in situ stresses, respectively, and θ is the angle between hydraulic fracture and natural fracture. According to this equation, the critical fissure opening pressure can be written as

$$p_c = \frac{1}{\alpha_f} [(2\nu p + \sigma_{\max}) \sin^2 \theta + (p + \sigma_{\min}) \cos^2 \theta]. \quad (16)$$

After the natural fracture opens, its hydraulic aperture increment associated with the changes in fluid pressure may be defined empirically as²⁴

$$db/dp_f = -\chi b, \quad (17)$$

where χ is a small constant characterizing the compliance of a natural fracture with respect to pressure change. Although Eq. (17) is usually used for closed fractures,²⁴ it is also applicable for completely open fractures, which is the case focused on here. This can be achieved by relating the relative change in fracture aperture, db/b , to the change in fluid pressure, dp_f , through a compliance-related coefficient χ . Compliance of natural fractures is of the order of $10^{-10} - 10^{-12}$ m/Pa,²⁵ and the aperture in dilation could be of the order of several millimeters. Therefore, a reasonable value for the constant χ should be $\sim 10^{-7} - 10^{-9}$ Pa⁻¹. By integrating, the hydraulic aperture of the natural fracture can be expressed as

$$b = \begin{cases} b_0 & p_f < p_c \\ b_0 \exp(-\chi \sigma_n^e) & p_f > p_c \end{cases}, \quad (18)$$

where b_0 is the initial natural fracture aperture. The dynamic porosity and permeability of the natural fracture system can be calculated, respectively, as^{26,27}

$$\phi_f = \phi_{f0} \frac{b}{b_0}, \quad (19)$$

$$k_f = k_{f0} \left(\frac{b}{b_0} \right)^3 \begin{bmatrix} \cos^2 \theta & \sin \theta \cos \theta \\ \sin \theta \cos \theta & \sin^2 \theta \end{bmatrix}. \quad (20)$$

Eqs. (13)–(16) and (18)–(19) give the complete set of the governing equations for the leakoff process in a dual porosity medium. By solving this set of equations, the leakoff velocity in Eq. (5) can be calculated by

$$u = 2 \left(-\frac{k_m}{\mu} \nabla p_m - \frac{k_f}{\mu} \nabla p_f \right) \quad (21)$$

at the walls of the hydraulic fracture, where the factor 2 accounts for leakoff through both walls of the fracture.

2.3. Governing equations for proppant transport

The presence of fluid-pressure-sensitive natural fractures will accelerate the leakoff process and exhibit a profound influence on the ability to drive a dominant hydraulic fracture or fracture network in naturally fractured reservoirs. This will in turn significantly influence the ability to infuse proppants in fractures that deeply penetrate the reservoir. In this section, we consider a proppant transport model within a propagating fracture which accommodates the effect of fracture dilation on leakoff as this directly influences the pressure gradient within the fracture and the ability of the fracturing fluid to carry the proppant load.

After introducing proppant, the mixture of fluid and particles forms a slurry with a behavior different from that of a pure fracturing fluid (governed by Eqs. (3) and (5)). The 1D mass balance equations for the slurry and proppant are given as

$$\frac{\partial \bar{q}^s}{\partial x} + \frac{\partial \bar{w}}{\partial t} + u = 0, \quad (22)$$

$$\frac{\partial \bar{q}^p}{\partial x} + \frac{\partial \bar{w}c}{\partial t} + S_{leakoff} = 0, \quad (23)$$

where $\bar{c} = c/c_{\max}$ is the normalized volumetric concentration of the proppant (with $c_{\max} = 0.585$ as the maximum allowable concentration), $S_{leakoff} = u\bar{c}H(b - 2Na)$ is the proppant leakoff rate into the natural fractures (here proppant is assumed to leakoff at the same velocity as fracturing fluid), with $H(\cdot)$ denoting the Heaviside step function, and \bar{q}^s and \bar{q}^p represent respectively the average slurry and proppant fluxes over the fracture height. The fluxes can be defined as

$$\bar{q}^s = -\frac{\bar{w}^3}{\pi^2 \mu} \hat{Q}^s \left(\bar{c}, \frac{\bar{w}}{a} \right) \frac{\partial p}{\partial x}, \quad (24)$$

$$\bar{q}^p = B \left(\frac{\bar{w}}{a} \right) \hat{Q}^p \left(\bar{c}, \frac{\bar{w}}{a} \right) \bar{q}^s, \quad (25)$$

where a is the particle radius, B is a blocking function, \hat{Q}^s and \hat{Q}^p are two dimensionless functions of proppant concentration and aperture.^{28,29}

The blocking function B accounts for proppant bridging and is described as

$$B \left(\frac{\bar{w}}{a} \right) = \frac{1}{2} H \left(\frac{\bar{w}}{2a} - N \right) H \left(N + 1 - \frac{\bar{w}}{2a} \right) \left(1 + \cos \left(\pi \left(N + 1 - \frac{\bar{w}}{2a} \right) \right) \right) + H \left(\frac{\bar{w}}{2a} - N - 1 \right) \quad (26)$$

where N represents a multiple of the particle diameter. Proppant bridging occurs when the fracture aperture is smaller than N times the proppant particle diameter. As an illustration, Fig. 3(a) shows the function B versus $\bar{w}/2a$ when $N = 3$.

Functions \hat{Q}^s and \hat{Q}^p are introduced by Dontsov and Peirce²⁹ based on an empirical constitutive model and expressed as

$$\hat{Q}^s \left(\bar{c}, \frac{\bar{w}}{a} \right) = Q^s(\bar{c}) + \frac{a^2}{\bar{w}^2} \bar{c} D, \quad (27)$$

$$\hat{Q}^p \left(\bar{c}, \frac{\bar{w}}{a} \right) = \frac{\bar{w}^2 Q^p(\bar{c})}{\bar{w}^2 Q^s(\bar{c}) + a^2 \bar{c} D}, \quad (28)$$

where Q^s and Q^p are dimensionless functions of normalized proppant concentration only and $D = 8(1 - c_{\max})^{\bar{\alpha}} / 3c_{\max}$ is a constant related to the permeability of the packed particles. In this study, $\bar{\alpha}$ is chosen to be 4.1 following Dontsov and Peirce.²⁸ The first term of Eq. (27) represents the reciprocal of the effective viscosity of the slurry. The slurry viscosity increases with an increase in the proppant concentration due to the interactions between particles and between particle and fluid. The second term of Eq. (27) accounts for Darcian flow within the porous medium. This term is trivial when proppant concentration is small and become significant when normalized proppant concentration is close to 1, as shown in Fig. 3(b). Thus, Eq. (24) is able to capture the transition from Poiseuille flow to Darcy filtration flow as the normalized proppant concentration increases from 0 to 1. The function \hat{Q}^p describes the proppant convection driven by the slurry flow. As can be seen from Fig. 3(c), \hat{Q}^p becomes zero when normalized proppant concentration reaches 1, indicating that an immobile bed is formed.

3. Numerical algorithm

The response of the system is evaluated by incorporating these constitutive relations into a numerical model. The system of equations is sequentially coupled and is solved in three steps: (i) solved for the leakoff velocity, i.e. coupling Eqs. (13), (14) and (21); (ii) solved for the propagation of the fracture, i.e. coupling Eqs. (3)–(5) and (7); and (iii) solved for proppant transport, i.e. Eq. (23). In this scheme, each system is solved while holding the primary variable from the other two systems of equations constant.

The system of governing equations is defined over the range $0 \leq x \leq l(t)$ which varies with the propagating fracture. To facilitate the numerical solution of this complex moving-boundary problem, a moving mesh is introduced to avoid adjusting the spatial discretization

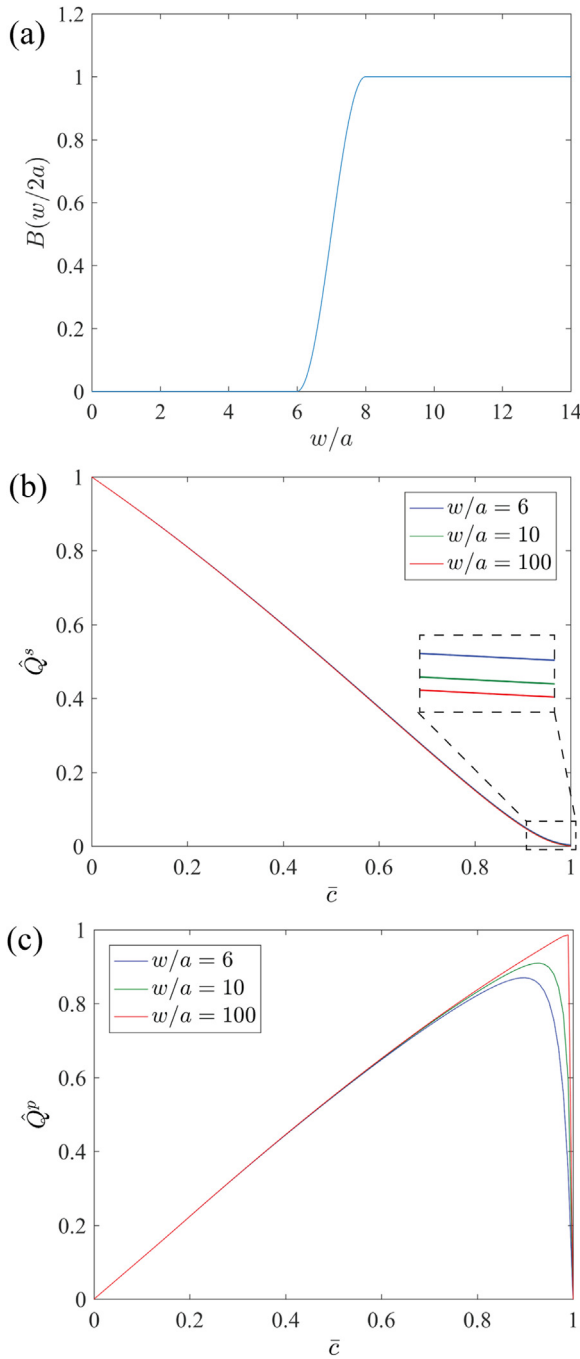


Fig. 3. (a) The blocking function when $N = 3$ and the functions (b) Q^s and (c) Q^p versus normalized proppant concentration for 3 specified values of the parameter.

at each time step. The equation systems for fracture propagation and proppant transport are reformulated in terms of the moving coordinate

$$\xi = \frac{x}{l(t)} \quad (29)$$

which remains in the range $[0, 1]$. The conversion of parameters from x to ξ requires a corresponding transformation of spatial and time derivatives written as

$$\frac{\partial(\cdot)}{\partial t} \Big|_x = \frac{\partial(\cdot)}{\partial t} \Big|_\xi - \xi \frac{l}{\partial \xi} \Big|_\xi, \quad (30)$$

$$\frac{\partial(\cdot)}{\partial x} \Big|_t = \frac{1}{l} \frac{\partial(\cdot)}{\partial \xi} \Big|_t, \quad (31)$$

where $\dot{l} = dl/dt$ is the velocity of fracture propagation. Under this transformation, the governing equation for fluid/slurry flow (Eqs. (5) or (22)) can be written as

$$\frac{\partial \bar{w}}{\partial t} - \xi \frac{\dot{l}}{l} \frac{\partial \bar{w}}{\partial \xi} + \frac{1}{l} \frac{\partial \bar{q}^s}{\partial \xi} + u = 0, \quad (32)$$

and the governing equation for proppant transport, i.e. Eq. (23) can be written as

$$\frac{\partial \bar{w} \bar{c}}{\partial t} - \xi \frac{\dot{l}}{l} \frac{\partial \bar{w} \bar{c}}{\partial \xi} + \frac{1}{l} \frac{\partial \bar{q}^p}{\partial \xi} + S_{leakoff} = 0. \quad (33)$$

The equation system for leakoff is solved at the natural scale.

As indicated earlier in this section, first, the leakoff velocity is determined for a given time step using the finite element method, and then Eq. (32) is solved to obtain the fracture geometry and fluid/slurry flow rate using an implicit finite difference scheme. Finally, the proppant distribution over the entire fracture length is updated by solving Eq. (33) using an explicit finite volume method. There is no restriction on the time step Δt when solving for the fracture propagation, while the time step for the proppant transport should be small enough to satisfy the Courant–Friedrichs–Lewy (CFL) condition.³⁰ To allow for arbitrarily large time steps for the whole algorithm, the time step Δt for Eq. (32) is subdivided into smaller time steps when solving for Eq. (33), each of which satisfies the CFL condition.

4. Numerical results

4.1. Model validation

Small and large time asymptotic solutions to the PKN model have been developed^{15,31} to describe limiting behavior of fracture propagation at sufficiently small and large times, respectively. To validate the established fracture propagation model, which accommodates the leakoff into a dual porosity medium, a simulation of fracture propagation without proppant transport is performed. The simulation results are compared with the small and large time asymptotic solutions^{15,31} where only the leakoff process into the natural fracture system (Eq. (14)) is considered without fluid transfer between matrix and natural fracture system. In addition, the natural fractures are set to be perpendicular to the hydraulic fracture and remain closed at all times, indicating constant permeability and porosity. As a result, a simplified 1-D single-porosity/permeability leakoff process is rigorously represented. This is comparable to the classical Carter leakoff model. The parameters used in this study are listed in Table 1.

Once the numerical solution is obtained, it is scaled as

$$\tau = \frac{t}{t_*}, \quad \gamma = \frac{l}{l_*}, \quad \Omega = \frac{\bar{w}}{w_*}, \quad (34)$$

where τ , γ and Ω are dimensionless time, fracture length and aperture,

Table 1

Input parameters for model validation case.

Parameter	Value
Injection rate, Q_0	0.004 m ³ /s
Fracture height, H	10 m
Plain strain Young's modulus, E'	25 GPa
Fluid dynamic viscosity, μ	0.001 Pa s
Fluid bulk modulus, K_w	2.2 GPa
Permeability of natural fracture system, k_f	1.5 × 10 ⁻¹⁷ m ²
Porosity of natural fracture system, ϕ_f	0.002
Initial formation pore pressure, p_0	6 MPa
Minimum in situ principle stress, σ_{min}	15 MPa

respectively. The three characteristic quantities are computed as

$$t_* = \frac{\pi^2 H^6 p_*^5}{4E'^4 \mu Q_0^2}, \quad l_* = \frac{\pi H^4 p_*^4}{4E'^3 \mu Q_0}, \quad w_* = \frac{\pi H p_*}{2E'}, \quad (35)$$

where $p_* = 1\text{MPa}$ is an introduced characteristic net pressure. Using the same scaling, the small time asymptotic solution^{15,31} can be written as

$$\gamma(\tau) = \gamma_{m0} \tau^{4/5}, \quad \Omega(\xi, \tau) = \Omega_{m0}(\xi) \tau^{1/5}, \quad \tau \ll 1, \quad (36)$$

with

$$\gamma_{m0} \cong 1.0006328, \quad (37)$$

$$\Omega_{m0} = \left(\frac{12}{5}\right)^{1/3} \gamma_{m0}^{2/3} (1 - \xi)^{1/3} \left(1 - \frac{1}{96}(1 - \xi)\right) + O((1 - \xi)^{7/3}). \quad (38)$$

The large time asymptotic solution^{15,31} can be written as

$$\gamma(\tau) = \gamma_{\bar{m}0} \tau^{1/2}, \quad \Omega(\xi, \tau) = \Omega_{\bar{m}0}(\xi) \tau^{1/8}, \quad \tau \gg 1, \quad (39)$$

with

$$\gamma_{\bar{m}0} = \frac{2}{\pi C}, \quad (40)$$

$$\Omega_{\bar{m}0}(\xi) = \left(\frac{8}{\pi C}\right)^{1/4} \left(\frac{2}{\pi} \xi \arcsin \xi + \frac{2}{\pi} \sqrt{1 - \xi^2} - \xi\right)^{1/4}, \quad (41)$$

$$C = \frac{C_l H^2 p_*^{3/2}}{\mu^{1/2} E' Q_0}, \quad (42)$$

where C_l is the leakoff coefficient. According to Carter leakoff theory,¹⁶ C_l can be calculated as

$$C_l = \Delta p \sqrt{\frac{k_f \phi_f}{\mu \pi K_w}}, \quad (43)$$

where Δp is the pressure differential between hydraulic fracture and formation. For this study, the leakoff coefficient C_l is calculated to be $7.91 \times 10^{-6} \text{ m/s}^{1/2}$.

The simulation starts at a non-dimensional time of $\tau = 10^{-7}$ and ends at $\tau = 10^5$ to ensure that it evolves from the small time to the large time similarity solution.^{15,31} Fig. 4(a) and (b) show the simulated evolution of fracture length $\gamma(\tau)$ and average width $\Omega(0, \tau)$ as a function of time τ , respectively, comparing these with the small time and large time asymptotics. The simulated solution faithfully follows the small time asymptotics at the beginning of the simulation (storage-dominated regime) and also the large time asymptotics at the end (leakoff-dominated regime). Comparisons of fracture profiles between numerical solution and similarity solutions for small and large time are shown in Fig. 4(c) and (d), respectively. In these two figures, the dashed lines with open circles represent the numerical solutions, while the red and blue solid lines depict the small time and large time similarity solutions, respectively. It can be seen that the simulated fracture profiles agree with the similarity solutions very well.

4.2. Simulations without proppant transport

A series of simulations without proppant transport were undertaken to explore the essential impacts of dual porosity flow around a propagating PKN fracture. Table 2 lists the input parameters for this study. The fracturing fluid is injected at a constant flow rate Q_0 for 3000 s. Then the pumping is stopped and the injected fluid is prevented from flowing back, i.e. the well is shut in. The analysis is carried out by considering (i) dual porosity leakoff with both fracture opening driven by fluid pressure and fluid transfer between fracture and surrounding matrix, and then (ii) a leakoff process only into a single natural fracture system with fracture opening but without fluid transfer between matrix

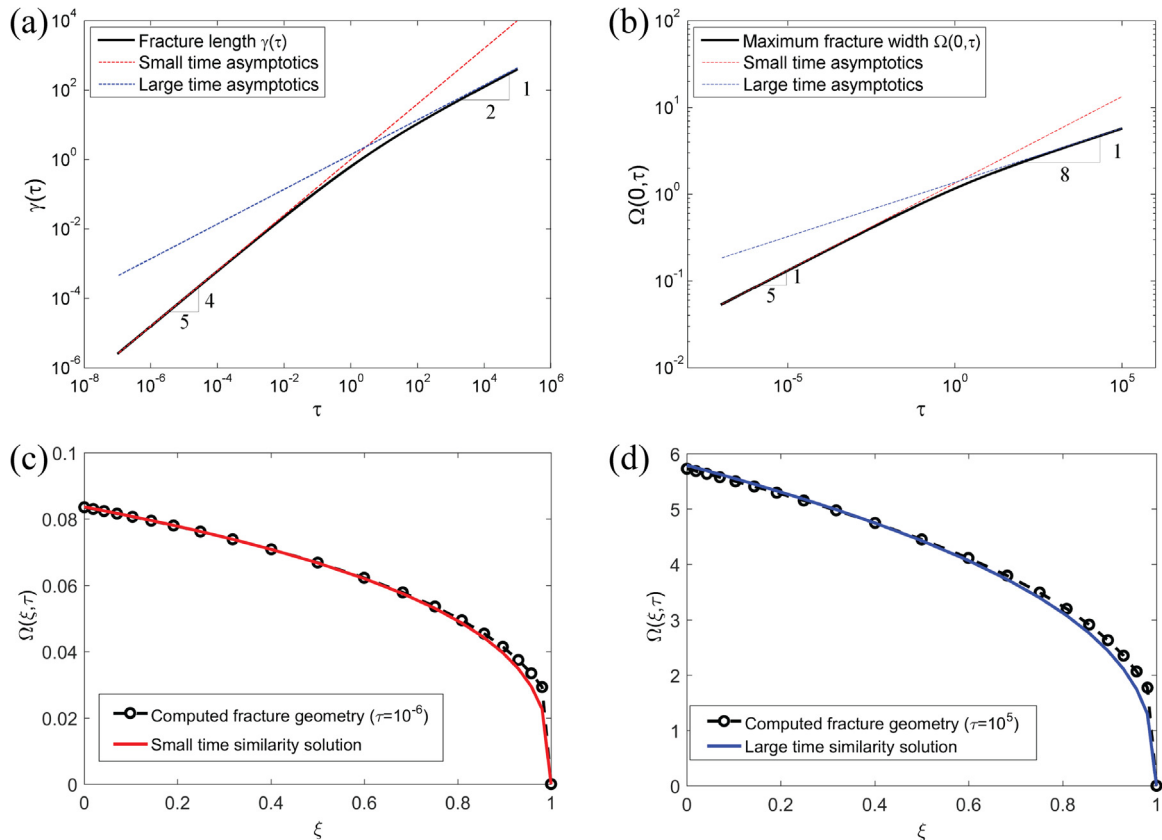


Fig. 4. Model validation: (a) comparison between simulated fracture length with small and large time asymptotics; (b) comparison between simulated fracture width at inlet with small and large time asymptotics; (c) comparison of fracture profile between numerical solution at and small time similarity solution; and (d) comparison of fracture profile between numerical solution at and large time similarity solution.

Table 2
Parameters for simulations without proppant transport.

Parameter	Value
Injection rate, Q_0	0.004 m ³ /s
Fracture height, H	10 m
Plain strain Young's modulus, E'	25 GPa
Poisson's ratio, ν	0.2
Fluid dynamic viscosity, μ	0.2 Pa s
Fluid bulk modulus, K_w	2.2 GPa
Initial permeability of natural fracture system, k_{f0}	3.25×10^{-15} m ²
Initial porosity of natural fracture system, ϕ_{f0}	0.002
Fracture spacing, s	0.2 m
Biot coefficient, α_f	0.8
Permeability of matrix, k_m	1.48×10^{-17} m ²
Porosity of matrix, ϕ_m	0.06
Initial formation pore pressure, p_0	6 MPa
Minimum in situ principle stress, σ_{min}	15 MPa
Maximum in situ principle stress, σ_{max}	16 MPa
Compliance coefficient of fractures, χ	3×10^{-7} 1/Pa
Angle between NFs and HF, θ	$\pi/2$

and fracture, and finally (iii) a single-porosity leakoff with constant formation permeability and porosity (referred to as Carter leakoff).

The evolution of fracture length and average width at inlet with time for the three cases mentioned above are shown in Fig. 5, with the dashed lines indicating the time when the well is shut in. It can be observed that the dual porosity medium, where fracture permeability is

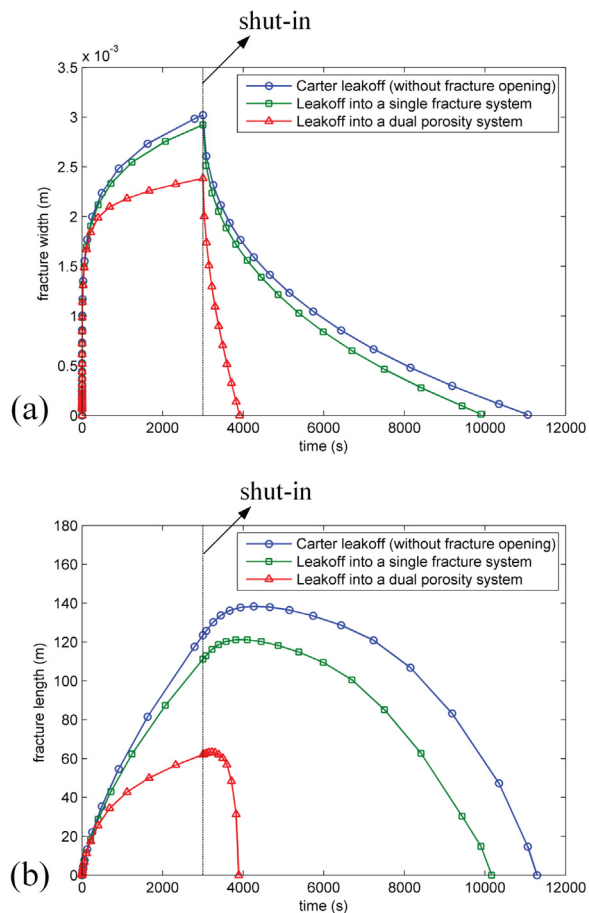


Fig. 5. Evolution of (a) fracture length and (b) average width at inlet with (i) leakoff into a single natural fracture system without fracture opening (Carter leakoff), (ii) leakoff into a single natural fracture system with fracture opening, and (iii) leakoff into a dual porosity system. (The black lines indicate the time when the well is shut in.).

a strong function of applied fluid pressure, results in a reduced length of the propagating fracture (Fig. 5(a)) due to the fugitive fluid leakoff from the fracture into the surrounding formation and that this in turn results in a reduced maximum width (Fig. 5(b)) during the treatment. After shut-in, the fracture length and width decrease more quickly for the dual porosity medium than the other two cases due to the faster leakoff. Fig. 6 shows the evolution of pore pressure for matrix and natural fracture system and fracture permeability ratio at a specified location ($x = 7$ m and $y = -7$ m) in the formation during the treatment. It can be seen that the pressure within the natural fractures builds more quickly than the matrix due to a higher permeability, and that the natural fractures begin to dilate when the fluid pressure reaches the critical fracture opening pressure, as indicated by the increase of the permeability in Fig. 6(b). A reduction of the fluid pressure within natural fractures follows shut-in due to the cessation of fluid supply, and this in turn results in a sudden drop of the fracture permeability, implying that the fracture closure results from the increase in normal effective stress. Fig. 7 displays the pore pressure distribution within the natural fracture system when the well is shut in. It is apparent that fluid travels for a longer distance in the region close to wellbore, i.e. the region where x is close to 0, due to the earlier arrival time of the fracture tip and the higher permeability resulting from the dilation of the natural fracture.

Two parametric studies were performed to examine the effect of the orientation and spacing of natural fractures on the resulting PKN fracture geometry. First, four cases with different angles between hydraulic fracture and natural fractures, θ , were conducted where the spacing between the natural fractures remains constant ($s = 0.2$ m). And then, several cases with different spacings between the natural fractures were simulated where θ was kept at $\pi/2$. The other parameters for these two parametric studies are listed in Table 2. Fig. 8 shows the evolution of fracture length and average width at inlet for four specified values of the angle between the main PKN fracture and natural fractures. It can be seen that the length and width of the hydraulic fracture increase as the angle θ decreases. This results because the leakoff process is moderated by the orientation of the natural fractures in the formation where the permeability increase is strongly influenced by the inclination of the fractures relative to the stress field – and this results in further feedbacks on the fracture length (Fig. 8(a)) and fracture width (Fig. 8(b)) of the main PKN fracture. Note that this model assumes a planar hydraulic fracture which always crosses the natural fractures directly – in certain cases the hydraulic fracture may divert into the natural fracture when the angle θ is small and this may result in stunted growth of the hydraulic fracture.³² Fig. 9 shows the main PKN fracture length at shut-in

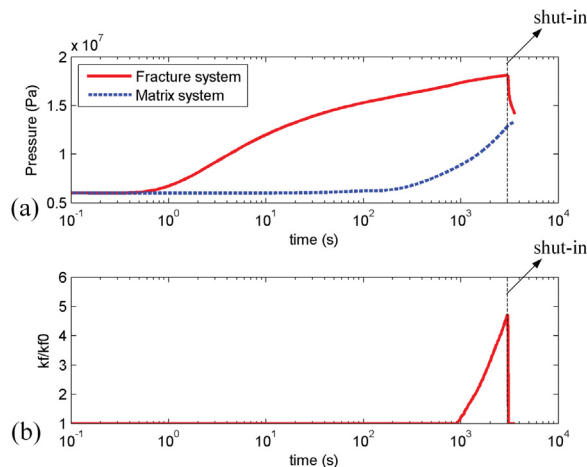


Fig. 6. (a) Evolution of fluid pressure and (b) fracture permeability ratio with time in fracture and matrix system at a specific location ($x = 7$ m and $y = -7$ m). (The black lines indicate the time when the well is shut in.).

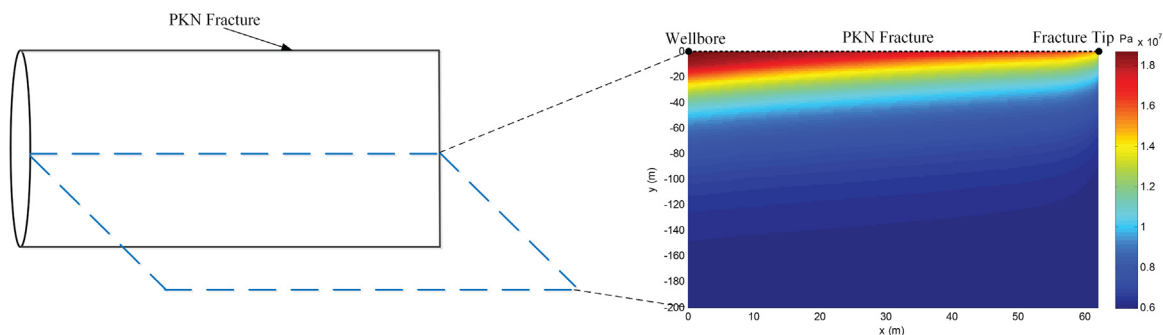


Fig. 7. Fluid pressure distribution of natural fracture system when the pumping stops.

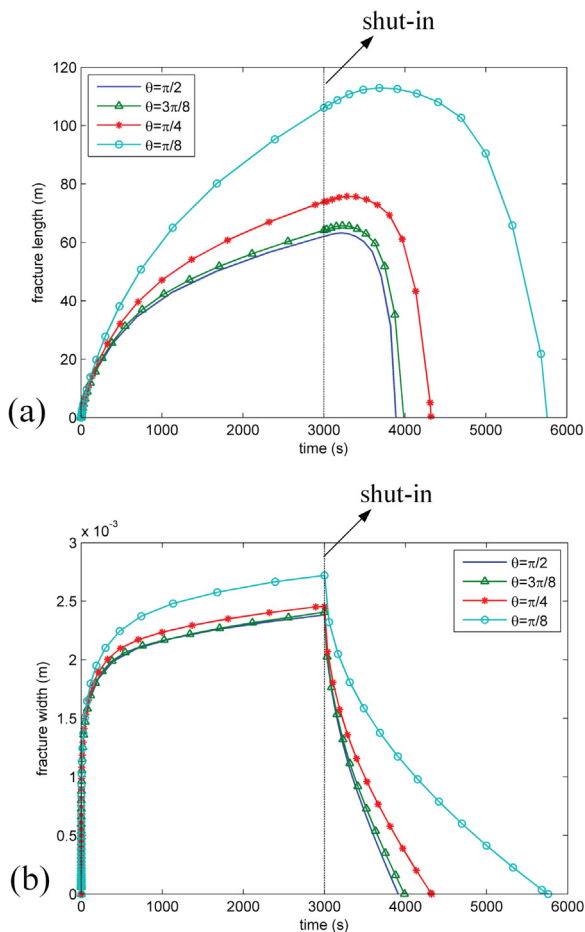


Fig. 8. Evolution of (a) fracture length and (b) average width at inlet with different angles between hydraulic fracture and natural fractures. (The black lines indicate the time when the pumping stops).

as a function of spacing of natural fractures. The PKN fracture length increases with an increase of the spacing of the natural fractures. This is due to small spacing between natural fractures enabling large contact areas between matrix and natural fracture system, which in turn accelerates the leakoff process and result in short main PKN fracture lengths.

4.3. Simulations with proppant transport

The foregoing analysis has illustrated that the presence of fluid-pressure-sensitive natural fractures exhibits a profound influence on the ability to drive a dominant PKN fracture in naturally fractured reservoir. This observation is important as this limits the maximum load

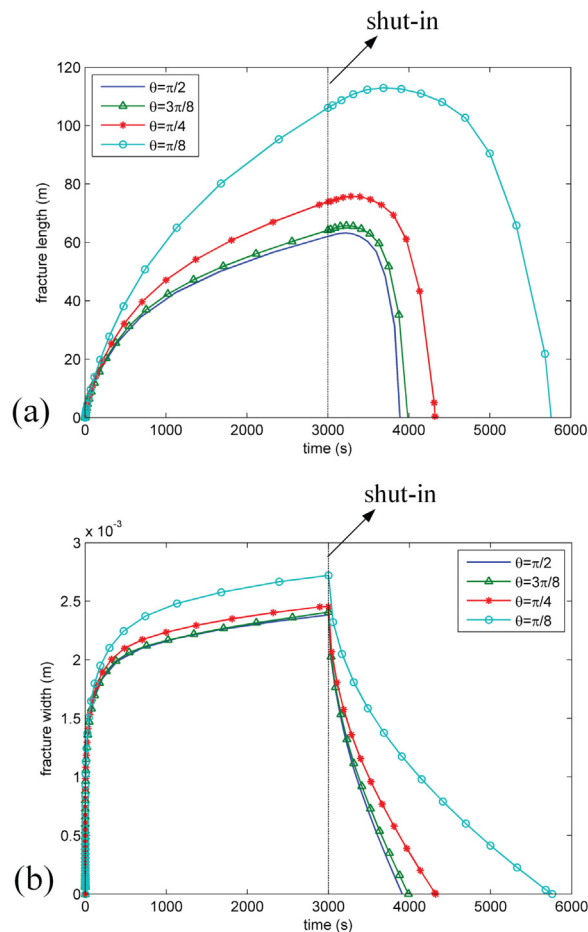


Fig. 9. Fracture length at the end of pumping as a function of natural fractures spacing.

of proppant that may be carried into the fracture and may compromise the ultimate efficiency of the final hydraulic fracture in relation to gas recovery. In this section, several cases are investigated to explore the impact of dual porosity leakoff on proppant transport. In these

Table 3
Parameters for simulations with proppant transport.

Case No.	Initial permeability of natural fracture system, k_{f0}	Fracture spacing, s	Proppant particle radius, a
1	$3.25 \times 10^{-15} \text{ m}^2$	0.5 m	$2 \times 10^{-4} \text{ m}$
2	$3.25 \times 10^{-13} \text{ m}^2$	0.5 m	$2 \times 10^{-4} \text{ m}$
3	$3.25 \times 10^{-13} \text{ m}^2$	20 m	$2 \times 10^{-4} \text{ m}$
4	$3.25 \times 10^{-13} \text{ m}^2$	20 m	$1 \times 10^{-4} \text{ m}$

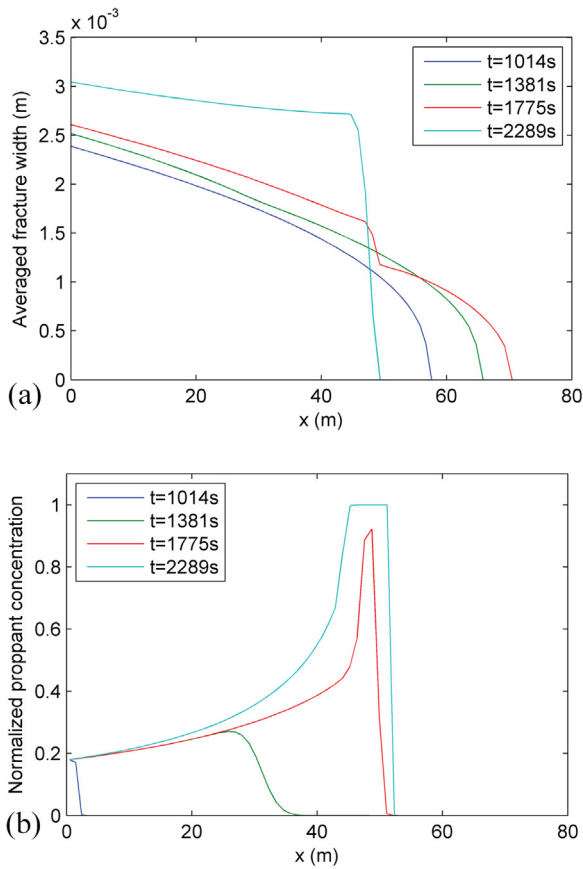


Fig. 10. (a) Fracture profiles and (b) the proppant concentration at different times of Case 1.

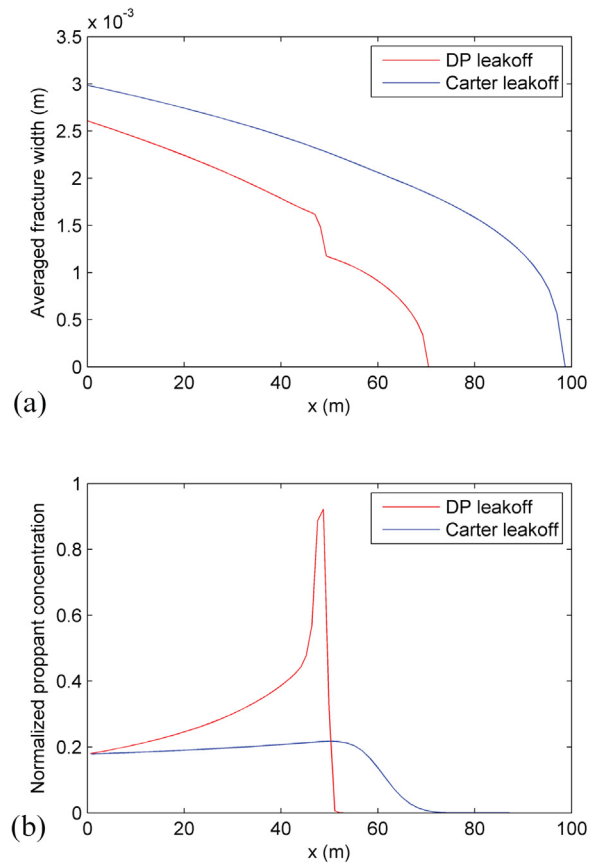


Fig. 12. Comparisons of (a) fracture profiles and (b) proppant concentration distribution at a specified time $t = 1775$ s between cases with dual porosity leakoff and Carter leakoff.

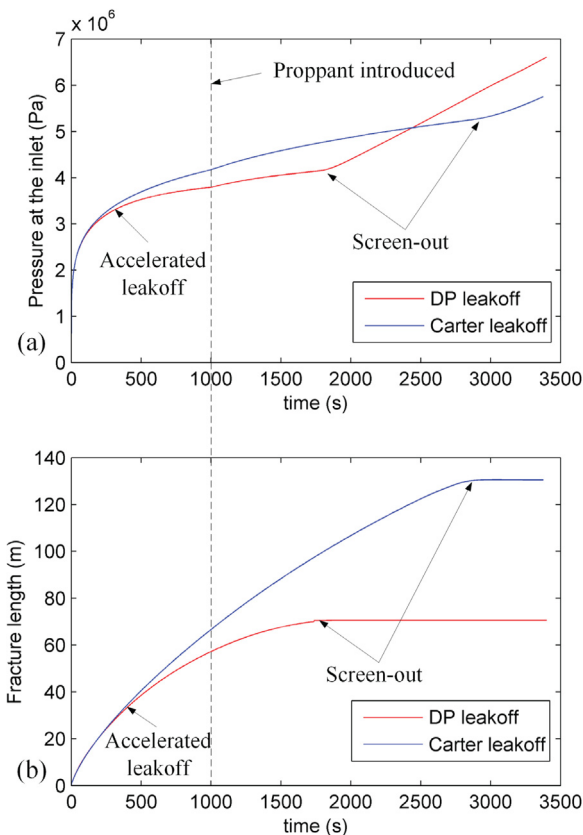


Fig. 11. (a) Inlet pressure and (b) fracture length histories for Case 1 (DP leakoff) and the reference simulation with Carter leakoff.

simulations, the main PKN fractures are driven by pure fracturing fluids until $t = 1000$ s, i.e. the pad time is 1000 s, and thereafter proppant is introduced forming a slurry comprising fracturing fluids and proppant particles. The simulations are stopped following screen-out. Proppant is introduced at a normalized volumetric concentration of 0.2. It is assumed that screen-out occurs when the fracture width is smaller than three particle diameters ($N = 3$). The initial permeability of the dual porosity medium, the spacing of the natural fractures and the radii of the proppant particles for the different cases are given in Table 3. The other input parameters are as listed in Table 2.

Case 1 is a standard case with dual porosity leakoff with Fig. 10 showing the simulated fracture profiles and proppant concentration at different times. At the beginning of the simulation, proppant particles transport from the wellbore towards the fracture tip, driven by the fluid flow. When the proppant reaches the tip region, where the fracture width is relatively small, they begin to accumulate - ultimately undergoing a sudden increase in the proppant concentration representing screen-out. After that, only a small fraction of the fracturing fluid is able to infiltrate through the packed bed into the tip region, while the rest is retained behind the bed resulting in fracture inflation, as apparent in Fig. 10(a). This observation is also supported by the pressure and length histories shown in Fig. 11. There is a slight increase in the fluid pressure at the inlet after proppant is introduced. This may be caused by the notable change in slurry viscosity. The pressure then builds (Fig. 11(a)) and the fracture stops propagating (Fig. 11(b)) when screen-out occurs. Note that the steps in fracture width that occur upon screenout (shown in Fig. 10(a)) result from the local elasticity equation, i.e. Eq. (4), which might not be rigorously applicable here. These steps should actually be smoother if a non-local elasticity equation is used.¹⁰

In order to examine the effect of dual porosity leakoff on proppant

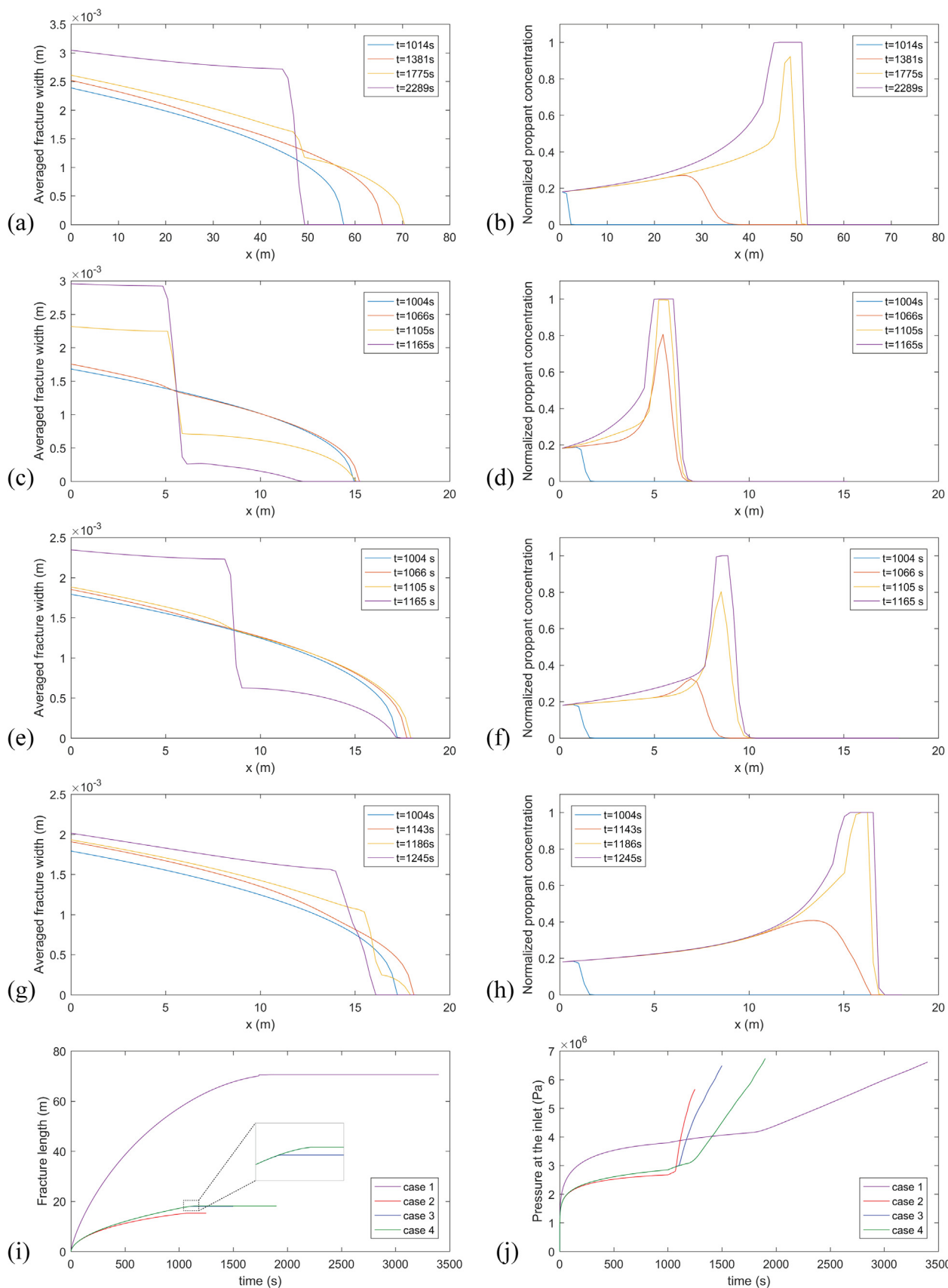


Fig. 13. Simulation results of Case 1–4: (a) fracture profiles and (b) the proppant concentrations at different times of Case 1; (c) fracture profiles and (d) the proppant concentrations at different times of Case 2; (e) fracture profiles and (f) the proppant concentrations at different times of Case 3; (g) fracture profiles and (h) the proppant concentrations at different times of Case 4; (i) variation of the pressure at the inlet and (j) fracture length versus time for Case 1–4.

Table 4
Initial natural fracture apertures for Case 1–4, evaluated from initial permeability.

Case no.	Initial natural fracture aperture, b_0	Ratio of initial fracture aperture and proppant particle diameter, $b_0/2a$
1	2.69×10^{-5} m	0.0673
2	1.25×10^{-4} m	0.3123
3	4.27×10^{-4} m	1.0682
4	4.27×10^{-4} m	2.1363

transport, a reference simulation with Carter leakoff is performed in which the other parameters remain the same as Case 1. Fig. 12 shows the comparisons of fracture profiles and proppant concentration distributions at a specified time between the two simulations. The fracture for dual porosity leakoff is shorter and narrower than that for Carter leakoff due to the large leakoff volume, which in turn leads to an earlier screen-out of the proppant. As can be seen from Fig. 12(b), at $t = 1775$ s, for the dual porosity leakoff, the proppant concentration at $x = 50$ m, which is still 20 m away from the fracture tip, reaches the maximum allowed proppant concentration, while for Carter leakoff the particles are able to continue advancing until they arrive at the tip region. Comparisons of pressure and fracture length histories are shown in Fig. 11. Again, accelerated leakoff is observed at $t \sim 400$ s for the dual porosity leakoff resulting from the dilation of the natural fractures. Also observed is that screen-out occurs much earlier for the dual porosity case as indicated by a faster rise in the pressure at inlet (Fig. 11(a)) and an earlier arrest in fracture length growth (Fig. 11(b)).

In Case 2, the permeability of the natural fracture system is 2 orders-of-magnitude larger than that of Case 1, with the simulation results shown in Fig. 13(c) and (d) (results of Case 1 are replotted in Fig. 13(a) and (b) to facilitate comparison). Apparent is that, due to the large leakoff rate, the fracture is both short and narrow (~ 15 m in length and ~ 1.7 mm in width) immediately before the proppant is introduced. This results in a premature proppant screen-out at ~ 1070 s after which the fracture propagation arrests and instead inflates in width. Conversely, with reduced leakoff (Case 1), the fracture is free to propagate until ~ 1775 s. In Case 3 (Fig. 13(e) and (f)), the spacing of the natural fracture system is increased to 20 m while all other parameters are kept the same as Case 2. Results show that proppant screen-out is delayed and a larger fraction of the fracture is propped for the lower leakoff of Case 3 relative to Case 2. This is due to that the larger fracture spacing (Case 3) reduces contact areas between matrix and natural fracture system which decelerates the leakoff and in turn results in a longer and wider driven fracture, as has been illustrated in the previous section. Case 4 (Fig. 13(g) and (h)) explores behavior for a proppant particle

size that is half of that of Case 3. Results show that smaller diameter proppant is able to reach the fracture tip more easily, resulting in later screen-out and with most of the fracture being propped. The variation of the pressure at the inlet and the fracture length versus time for Case 1–4 are shown in Fig. 13(i) and (j) where the rapid pressure buildup and the constant fracture length indicate proppant screen-out. It is apparent that Case 1 (reduced leakoff) returns the longest fracture and most delayed proppant screen-out, followed by Case 4 (small porppant with leakoff) and Case 3 (standard proppant with widely spaced natural fractures), with Case 2 (standard proppant closely space natural fractures) exhibiting the shortest fracture and earliest proppant screen-out.

The dilation of the pre-existing natural fractures during hydraulic fracturing treatment may result in active flow within the fracture networks, increase the effective stimulated reservoir volume (SRV), and improve the effectiveness of the treatment.³³ However, the active network (the SRV that is open for gas flow) may be smaller than the SRV since some parts of the natural fractures are left unpropped and will close following treatment. Therefore, estimating the propped volume of the natural fractures is crucial in evaluating well performance. By using the proposed model and assuming that the proppant travel at the same velocity as the fracturing fluids, the proppant travel distance away from the main fracture, $L(x,t)$, may be obtained by tracking the proppant front as follows

$$L(x, t) = L_0(x, t_0) + \int_{t_0}^t [v_{nf}(x, L_0(x, t'), t') \times H(b(x, L_0(x, t'), t') - 2Na)] dt', \tag{44}$$

where $L_0(x,t_0)$ is the proppant travel distance at last time step, v_{nf} is the average linear velocity along the direction of the natural fractures, b is the aperture of the natural fractures, and $H(\cdot)$ is the Heaviside step function. Eq. (44) can be simply viewed as an integral of travel velocity over travel time. For Case 1–4, the initial natural fracture apertures, b_0 , can be back-calculated from the initial fracture permeability, k_{f0} , and spacing, s , using the cubic law as²⁶

$$b_0 = \sqrt[3]{12sk_{f0}}, \tag{45}$$

with the results listed in Table 4. In Case 1–3 (standard proppant diameters with various forms of dual porosity leakoff), the natural fractures are too narrow to allow the proppant particles to migrate into the natural fractures – although the fractures do dilate during the treatment. Conversely, for Case 4 (proppant of halved-diameter), the proppant is able to enter into the natural fractures when the fracture is dilated to $b > 6a$. Fig. 14 shows the extent of the region of propped natural fractures (red color) at the completion of the stimulation. The proppant travels furthest in the region closest to the wellbore where the dilation of the fractures is greatest (highest fluid pressure) and where

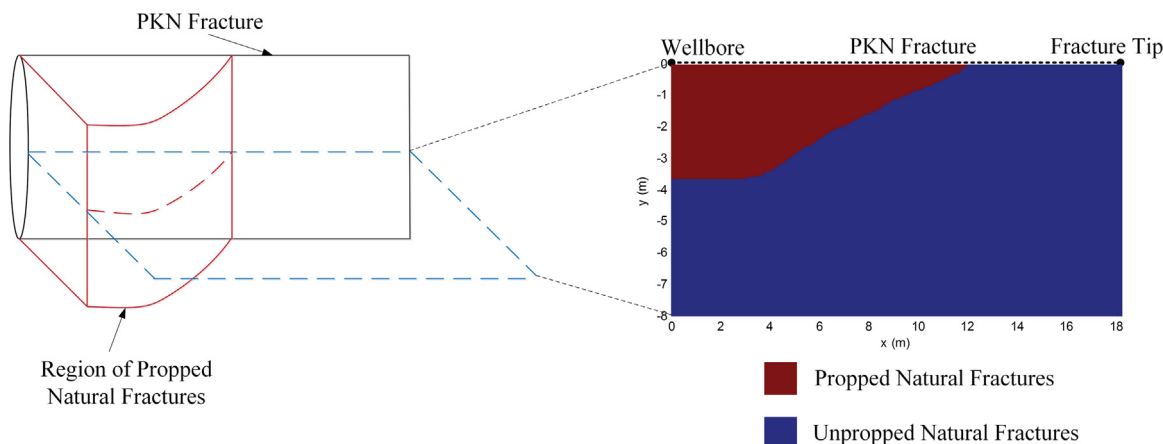


Fig. 14. Regions of propped (red color) and unpropped (blue color) natural fractures for Case 4 at the completion of the stimulation. (For interpretation of the references to color in this figure legend, the reader is referred to the web version of this article.).

the advective fluid velocities (largest fluid pressure gradients) are highest. No proppant enters into the natural fractures in the region closest to the fracture tip due to minimal dilation and low pressure gradients – the converse of conditions close to the wellbore. The propped natural fractures may be more beneficial to the effective production of hydrocarbon than the un-propped fractures³⁴ once stimulation is arrested and fractures compact as pressures drop below in situ stress magnitudes.

5. Conclusions

We present a coupled hydraulic fracturing model that is capable of accommodating leakoff from an evolving PKN fracture into a dual porosity medium. The model accommodates natural fractures that intersect the main PKN fracture and dilate and contribute flow from (and then to) that PKN fracture. These fractures are fluid pressure sensitive and dilate in response to the inflation of the fracture – following the appropriate permeability and leakoff response for the medium. A proppant transport model is included to study the proppant concentration distribution concurrent with the fracture propagation.

The simulation results illustrate that leakoff into a dual porosity medium, where fracture permeability is a strong function of applied fluid pressure, results in a reduced length and width of the propagating fracture. This is due to the fugitive fluid leakoff from the fracture into the surrounding formation. This behavior is moderated by the orientation and spacing of the natural fractures in the formation. Here, the permeability increase is strongly influenced by the inclination of the fractures relative to the stress field and the fluid transfer volume between matrix and natural fracture system is largely controlled by the

spacing of the natural fractures.

The impact of dual porosity leakoff is significant as this limits the maximum load of proppant that may be carried into the fracture. Screen-out of proppant occurs much earlier for the case with dual porosity leakoff, and the ability to infuse proppants in fluid-driven fractures penetrating large distances from the injection wellbore is further limited by this premature screen-out, which may compromise the ultimate efficiency of the final hydraulic fracture relative to gas recovery. Reduced propagation and premature screen-out are limited by low permeability and large spacing of natural fractures. This results from reducing the leakoff rate which in turn results in a wider main fracture and delays the occurrence of proppant screen-out. The reach of the effective production network, which is related to the propped natural fractures, can also be estimated by using the proposed model. The proppant travels furthest in the region closest to the wellbore where the dilation of the fractures is greatest and where the advective fluid velocities are highest, while proppant may not be able to enter into the natural fractures in the region closest to the fracture tip due to minimal dilation and low pressure gradients. Only the propped natural fractures contribute to the effective production from the network once stimulation is arrested and fractures reseal under reversed pressure magnitudes.

Acknowledgements

This work is the result of support from DOE under the Small Business Innovative Research (SBIR) program (grant number: DE-SC0013217). This support is gratefully acknowledged.

Appendix A. Derivations of governing equations for leakoff process in a dual porosity medium

The following provides the background derivations of Eqs. (13) and (14). Substituting Eqs. (11) and (12) into Eqs. (8) and (9) yields

$$\frac{\partial M_m}{\partial t} + \nabla \cdot \left(-\rho \frac{k_m}{\mu} \nabla p_m \right) = \omega(p_f - p_m)\rho, \tag{A-1}$$

and

$$\frac{\partial M_f}{\partial t} + \nabla \cdot \left(-\rho \frac{k_f}{\mu} \nabla p_f \right) = -\omega(p_f - p_m)\rho. \tag{A-2}$$

Since the fluid masses are $M_m = \rho\phi_m$ and $M_f = \rho\phi_f$, Eqs. (A-1) and (A-2) can be rewritten as

$$\rho \frac{\partial \phi_m}{\partial t} + \phi_m \frac{\partial \rho}{\partial t} + \nabla \cdot \left(-\rho \frac{k_m}{\mu} \nabla p_m \right) = \omega(p_f - p_m)\rho, \tag{A-3}$$

and

$$\rho \frac{\partial \phi_f}{\partial t} + \phi_f \frac{\partial \rho}{\partial t} + \nabla \cdot \left(-\rho \frac{k_f}{\mu} \nabla p_f \right) = -\omega(p_f - p_m)\rho. \tag{A-4}$$

Fluid bulk modulus, K_w , is defined as

$$\frac{1}{K_w} = \frac{1}{\rho} \frac{\partial \rho}{\partial p}, \tag{A-5}$$

thus the derivative of fluid density with respect to time can be expressed as

$$\frac{\partial \rho}{\partial t} = \frac{\partial \rho}{\partial p} \frac{\partial p}{\partial t} = \frac{\rho}{K_w} \frac{\partial p}{\partial t}. \tag{A-6}$$

Solid grain bulk modulus, K_s , is defined as

$$\frac{1}{K_s} = -\frac{1}{V_s} \frac{\partial V_s}{\partial p_m} = -\frac{1}{V - V_p} \frac{\partial (V - V_p)}{\partial p_m} = \frac{1}{1 - \phi_m} \frac{\partial \phi_m}{\partial p_m}, \tag{A-7}$$

where V_s , V_p and V are volume of solid grain, volume of pore space and total volume, respectively. The derivative of the matrix porosity with respect to time can be expressed as

$$\frac{\partial \phi_m}{\partial t} = \frac{\partial \phi_m}{\partial p_m} \frac{\partial p_m}{\partial t} = \frac{1 - \phi_m}{K_s} \frac{\partial p_m}{\partial t}. \tag{A-8}$$

Substituting Eqs. (A-6) and (A-8) into Eqs. (A-3) and (A-4) gives

$$\left(\frac{\phi_m}{K_w} + \frac{1 - \phi_m}{K_s}\right) \frac{\partial p_m}{\partial t} + \nabla \cdot \left(-\frac{k_m}{\mu} \nabla p_m\right) = \omega(p_f - p_m), \tag{A-9}$$

and

$$\frac{\partial \phi_f}{\partial t} + \frac{\phi_f}{K_w} \frac{\partial p_f}{\partial t} + \nabla \cdot \left(-\frac{k_f}{\mu} \nabla p_f\right) = -\omega(p_f - p_m). \tag{A-10}$$

Appendix B. Equivalent carter leakoff coefficient

It may be beneficial to have an equivalent Carter leakoff coefficient to represent the leakoff process into a pressure-sensitive dual porosity medium. This will be computationally time-saving since it can avoid spatial discretization of the formation surrounding the main PKN fracture. The fluid leakoff into a dual porosity medium consists of (i) fluid directly penetrating into the matrix, (ii) fluid flowing into natural fractures, and (iii) fluid transferring from natural fractures to the matrix. According to the Carter leakoff model, the rate of fluid directly penetrating into the matrix can be written as

$$u_1(x, t) = \frac{2C_l^m}{\sqrt{t - \tau(x)}}. \tag{A-11}$$

where $C_l^m = \Delta p \sqrt{\frac{k_m \phi_m}{\mu \pi k_w}}$ is a constant leakoff coefficient. If the fluid transfer from the natural fractures to the matrix is ignored, rate of fluid flowing into the natural fractures can be approximated as

$$u_2(x, t) = \frac{2C_l^f}{\sqrt{t - \tau(x)}}, \tag{A-12}$$

where $C_l^f = \Delta p \sqrt{\frac{k_f(p) \phi_f}{\mu \pi k_w}}$ is a variable leakoff coefficient due to the fact that the fracture permeability $k_f(p)$ as a function of net pressure, p , as shown in Eq. (20). Pressure p varies slowly with both t and x and use of an average value, \bar{p} , for net pressure in Eq. (45) may be acceptable.³ Fluid travel distance away from the main PKN fracture can be evaluated by integrating $\frac{1}{2}u_2 dt$ from 0 to $t - \tau(x)$, which is $2C_l^f \sqrt{t - \tau(x)}$. Thus, the leakoff rate resulting from fluid transfer from the natural fractures to the matrix can be approximately expressed as

$$u_3(x, t) = \frac{8v_{tr} C_l^f \sqrt{t - \tau(x)}}{b(\bar{p})}, \tag{A-13}$$

where $v_{tr} = \frac{k_m \Delta p}{\mu s/2}$ is the flow rate from the natural fractures to the matrix. Therefore, the total leakoff rate can be approximated as

$$u(x, t) = u_1(x, t) + u_2(x, t) + u_3(x, t) = \frac{2C_l^e}{\sqrt{t - \tau(x)}}, \tag{A-14}$$

where C_l^e is the equivalent Carter leakoff coefficient and is expressed as

$$C_l^e = C_l^m + C_l^f + \frac{8k_m \Delta p C_l^f [t - \tau(x)]}{sub(\bar{p})}. \tag{A-15}$$

References

1. Khristianovic SA, Zheltov YP. Formation of vertical fractures by means of highly viscous liquid. In: *Proceeding of the 4th World Pet Congr.*; 1955:579-586.
2. Perkins TK, Kern LR. Widths of hydraulic fractures. *J Pet Technol.* 1961;13(9):937-949. <http://dx.doi.org/10.2118/89-PA>.
3. Nordgren RP. Propagation of a vertical hydraulic fracture. *Soc Pet Eng J.* 1972;12(4):306-314. <http://dx.doi.org/10.2118/3009-PA>.
4. Greetesma J, de Klerk F. A rapid method of predicting width and extent of hydraulic induced fractures. *J Pet Technol.* 1969;21:1571-1581.
5. Adachi J, Siebrits E, Peirce A, Desroches J. Computer simulation of hydraulic fractures. *Int J Rock Mech Min Sci.* 2007;44(5):739-757. <http://dx.doi.org/10.1016/j.ijrmmms.2006.11.006>.
6. Rahman MM, Rahman MK. A review of hydraulic fracture models and development of an improved pseudo-3D model for stimulating tight oil/gas sand. *Energy Sources Part A Recover Util Environ Eff.* 2013;32(15):1416-1436. <http://dx.doi.org/10.1080/15567030903060523>.
7. Garagash DI, Detournay E. The tip region of a fluid-driven fracture in an elastic medium. *J Appl Mech.* 1999;67(1):183-192. <http://dx.doi.org/10.1115/1.321162>.
8. Detournay E. Propagation regimes of fluid-driven fractures in impermeable rocks. *Int J Geomech.* 2004;4(1):35-45. [http://dx.doi.org/10.1061/\(ASCE\)1532-3641\(2004\)4:1\(35\)](http://dx.doi.org/10.1061/(ASCE)1532-3641(2004)4:1(35)).
9. Adachi JI, Peirce AP. Near-tip asymptotic analysis of a pkn fluid-driven fracture with non-local elasticity equation. In: *ICF XI - Proceedings of the 11th International Conference Fract.*; (ii); 2005. <http://www.icf11.com/proceeding/EXTENDED/5153.pdf>.
10. Adachi JI, Peirce AP. Asymptotic analysis of an elasticity equation for a finger-like hydraulic fracture. *J Elast.* 2008;90(1):43-69. <http://dx.doi.org/10.1007/s10659-007-9122-4>.

11. Garagash DI. Plane-strain propagation of a fluid-driven fracture during injection and shut-in: asymptotics of large toughness. *Eng Fract Mech.* 2006;73(4):456-481. <http://dx.doi.org/10.1016/j.engfracmech.2005.07.012>.
12. Detournay E. Mechanics of hydraulic fractures. *Annu Rev Fluid Mech.* 2016;48(1):311-339. <http://dx.doi.org/10.1146/annurev-fluid-010814-014736>.
13. Ueda K, Kuroda S, Corporation I, Rodriguez-herrera A, Garcia-teijeiro X. Hydraulic fracture design in the presence of highly-stressed layers: a case study of stress interference in a multi-horizontal well pad. In: *SPE Hydraulic Fracturing Technology Conference and Exhibition.* Society of Petroleum Engineers; 2018.
14. Cohen C-E, Kresse O, Weng X. A new stacked height growth model for hydraulic fracturing simulation. In: *Proceedings of the 49th US Rock Mechanics/Geomechanics Symposium.* San Francisco: American Rock Mechanics Association; 2015.
15. Adachi JI, Detournay E, Peirce AP. Analysis of the classical pseudo-3D model for hydraulic fracture with equilibrium height growth across stress barriers. *Int J Rock Mech Min Sci.* 2010;47(4):625-639. <http://dx.doi.org/10.1016/j.ijrmmms.2010.03.008>.
16. Howard G, Fast CR. Optimum fluid characteristics for fracture extension? *Proc Am Pet Inst.* 1957:261-270 [doi:API-57-261].
17. Warpinski N. Hydraulic fracturing in tight, fissured media. *J Pet Technol.* 1991;43(2) <http://dx.doi.org/10.2118/20154-PA>.
18. Nolte KG, Smith MB. Interpretation of fracturing pressures. *J Pet Technol.* 1981;33(9):1,767-1,775. <http://dx.doi.org/10.2118/8297-PA>.
19. Gale JFW, Reed RM, Holder J. Natural fractures in the Barnett Shale and their importance for hydraulic fracture treatments. *Am Assoc Pet Geol Bull.* 2007;91(4):603-622. <http://dx.doi.org/10.1306/11010606061>.
20. Warren JE, Root PJ. The behavior of naturally fractured reservoirs. *Soc Pet Eng.* 1963. <http://dx.doi.org/10.2118/426-PA>.
21. Lim KT, Aziz K. Matrix-fracture transfer shape factors for dual-porosity simulators. *J*

- Pet Sci Eng.* 1995;13(3–4):169–178. [http://dx.doi.org/10.1016/0920-4105\(95\)00010-F](http://dx.doi.org/10.1016/0920-4105(95)00010-F).
22. Mora CA, Wattenbarger RA. Analysis and verification of dual porosity and CBM shape factors. *J Can Pet Technol.* 2009;48(2):17–21. <http://dx.doi.org/10.2118/09-02-17>.
 23. Zimmerman RW, Chen G, Hadgu T, Bodvarsson GS. A numerical dual-porosity model with semianalytical treatment of fracture/matrix flow. *Water Resour Res.* 1993;29(7):2127–2137. <http://dx.doi.org/10.1029/93WR00749>.
 24. Zhang X, Jeffrey RG, Thiercelin M. Mechanics of fluid-driven fracture growth in naturally fractured reservoirs with simple network geometries. *J Geophys Res Solid Earth.* 2009;114(12):1–16. <http://dx.doi.org/10.1029/2009JB006548>.
 25. Hobday C, Worthington MH. Field measurements of normal and shear fracture compliance. *Geophys Prospect.* 2012;60(3):488–499. <http://dx.doi.org/10.1111/j.1365-2478.2011.01000.x>.
 26. Robertson E, Christiansen R. A permeability model for coal and other fractured sorptive-elastic media. *SPE J.* 2008;11–13. <http://dx.doi.org/10.2118/104380-PA>.
 27. Lei G, Dong PC, Mo SY, Yang S, Wu ZS, Gai SH. Calculation of full permeability tensor for fractured anisotropic media. *J Pet Explor Prod Technol.* 2015;5(2):167–176. <http://dx.doi.org/10.1007/s13202-014-0138-6>.
 28. Dontsov EV, Peirce AP. Proppant transport in hydraulic fracturing: crack tip screen-out in KGD and P3D models. *Int J Solids Struct.* 2015;63:206–218. <http://dx.doi.org/10.1016/j.ijsolstr.2015.02.051>.
 29. Dontsov EV, Peirce a.P. Slurry flow, gravitational settling and a proppant transport model for hydraulic fractures. *J Fluid Mech.* 2014;760:567–590. <http://dx.doi.org/10.1017/jfm.2014.606>.
 30. LeVeque RJ. *Finite Volume Methods for Hyperbolic Problems.* Cambridge University Press; 2002. <http://dx.doi.org/10.1017/CBO9780511791253>.
 31. Kovalyshen Y, Detournay E. A reexamination of the classical PKN model of hydraulic fracture. *Transp Porous Media.* 2010;81(2):317–339. <http://dx.doi.org/10.1007/s11242-009-9403-4>.
 32. Zhang F, Dontsov E, Mack M. Fully coupled simulation of a hydraulic fracture interacting with natural fractures with a hybrid discrete-continuum method. *Int J Numer Anal Methods Geomech.* 2017. <http://dx.doi.org/10.1002/nag.2682>.
 33. Mayerhofer MJ, Lonon E, Warpinski NR, Cipolla CL, Walsler DW, Rightmire CM. What is stimulated reservoir volume? *SPE Prod Oper.* 2010;25(1):89–98. <http://dx.doi.org/10.2118/119890-PA>.
 34. Wang J, Elsworth D. Role of proppant distribution on the evolution of hydraulic fracture conductivity. *J Pet Sci Eng.* 2018;166:249–262. <http://dx.doi.org/10.1016/j.petrol.2018.03.040>.